

# Harvesting Low-Frequency (<5 Hz) Irregular Mechanical Energy: A Possible Killer Application of Triboelectric Nanogenerator

Yunlong Zi,<sup>†,‡</sup> Hengyu Guo,<sup>†,§,‡</sup> Zhen Wen,<sup>†,‡,‡</sup> Min-Hsin Yeh,<sup>†</sup> Chenguo Hu,<sup>§</sup> and Zhong Lin Wang<sup>\*,†,||</sup>

<sup>†</sup>School of Materials Science and Engineering, Georgia Institute of Technology, Atlanta, Georgia 30332, United States

<sup>§</sup>Department of Applied Physics, Chongqing University, Chongqing 400044, China

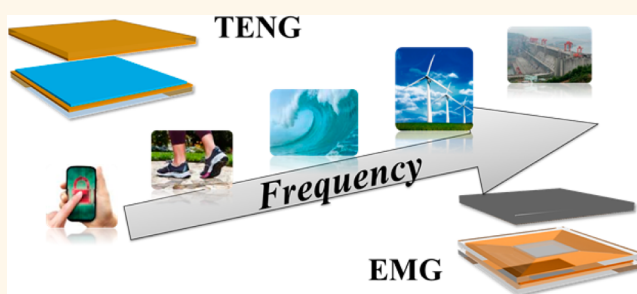
<sup>‡</sup>State Key Laboratory of Silicon Materials, School of Materials Science & Engineering, Cyrus Tang Center for Sensor Materials and Applications, Zhejiang University, Hangzhou 310027, China

<sup>||</sup>Beijing Institute of Nanoenergy and Nanosystems, Chinese Academy of Sciences; National Center for Nanoscience and Technology (NCNST), Beijing 100083, China

## S Supporting Information

**ABSTRACT:** Electromagnetic generators (EMGs) and triboelectric nanogenerators (TENGs) are the two most powerful approaches for harvesting ambient mechanical energy, but the effectiveness of each depends on the triggering frequency. Here, after systematically comparing the performances of EMGs and TENGs under low-frequency motion (<5 Hz), we demonstrated that the output performance of EMGs is proportional to the square of the frequency, while that of TENGs is approximately in proportion to the frequency. Therefore, the TENG has a much better performance than that of the EMG at low frequency (typically 0.1–3 Hz). Importantly, the extremely small output voltage of the EMG at low frequency makes it almost inapplicable to drive any electronic unit that requires a certain threshold voltage (~0.2–4 V), so that most of the harvested energy is wasted. In contrast, a TENG has an output voltage that is usually high enough (>10–100 V) and independent of frequency so that most of the generated power can be effectively used to power the devices. Furthermore, a TENG also has advantages of light weight, low cost, and easy scale up through advanced structure designs. All these merits verify the possible killer application of a TENG for harvesting energy at low frequency from motions such as human motions for powering small electronics and possibly ocean waves for large-scale blue energy.

**KEYWORDS:** triboelectric nanogenerator, electromagnetic generator, mechanical energy, low-frequency energy, energy harvesting



The development of a sensor network for big data and the Internet of Things is predicted to be the main driving technology for the future. Although the power required for operating a single electronic device is minimal, the number of such devices in the net is huge, in the range of trillions. Traditional power sources rely on batteries and supercapacitors, but they have limited lifetime, need replacement, and require maintenance. Energy harvesting technologies have been actively developed by converting ambient energy in the environment into electric power so that a device can be self-powered.<sup>1</sup> Due to its ubiquitous existence and abundant availability, mechanical energy is considered an ideal power source for energy harvesting by electromagnetic,<sup>2</sup> electrostatic,<sup>3</sup> triboelectric,<sup>4</sup> and piezoelectric<sup>5</sup> effects, among which electromagnetic generators (EMGs) and triboelectric nanogenerators (TENGs) are the two most efficient approaches. As the most classical technology, EMGs, based on Faraday's law of

electromagnetic induction, are currently used for powering small electronics and large-scale power generation. The TENG, based on coupling of triboelectrification and electrostatic induction as invented in 2012, is relatively new, but it has attracted a broad interest due to its high energy conversion efficiency, low cost, flexibility, and abundant choice of materials.<sup>6–9</sup>

The mechanical energy available in the environment usually has a frequency lower than 10 Hz, such as ocean waves, tides, and human motion.<sup>10,11</sup> Harvesting such low-frequency energy using an EMG may be ineffective, since the output power decays greatly with the decrease of frequency<sup>10</sup> and the output

**Received:** March 3, 2016

**Accepted:** April 14, 2016

**Published:** April 14, 2016

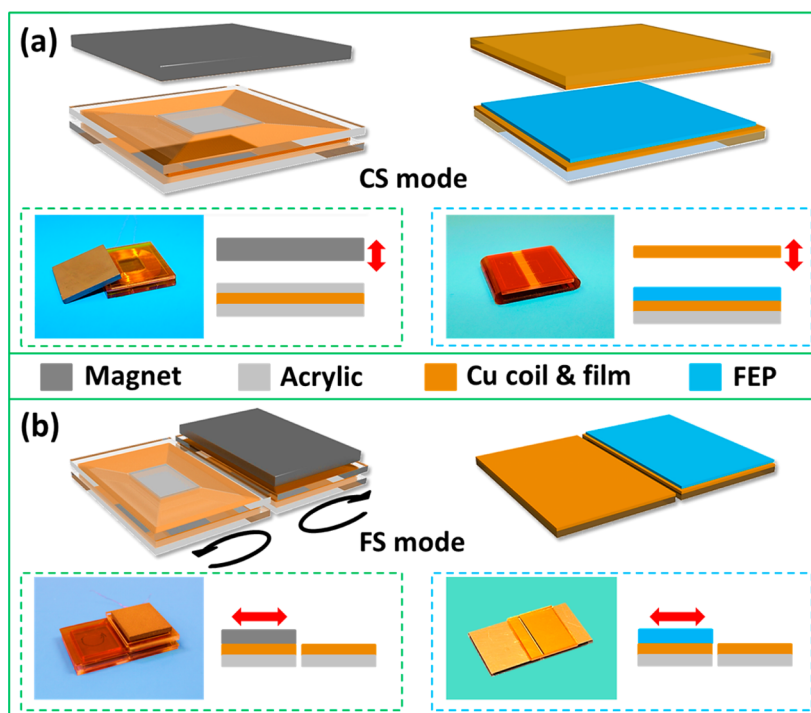


**Figure 1.** 3D schematics, photos, and cross-sectional views of a fabricated (a) CS mode of an EMG (left) and TENG (right) and (b) FS mode of an EMG (left) and TENG (right). The legend is shown above (b). In (b), the winding directions of Cu wires were marked for the FS mode EMG. The size and weight of EMGs and TENGs are listed in the [Experimental Methods](#).

voltage is rather low at low frequency. This is likely to be the reason that the conventional ac generator operates at 50–60 Hz. Although efforts have been devoted in recent years to improve the power output in the low-frequency range,<sup>10–18</sup> it is still difficult to utilize EMGs to effectively harvest mechanical energy in sub-10 Hz and even sub-1 Hz frequencies. TENG has been reported for energy harvesting from broadband-frequency mechanical energy sources such as vibrations,<sup>19–21</sup> human walking,<sup>22,23</sup> body motions,<sup>24–27</sup> and ocean waves.<sup>28–30</sup> Although a theoretical comparison between EMGs and TENGs has been performed by Zhang *et al.*,<sup>31</sup> a quantitative analysis between the two is still not available to reveal the frequency range in which a TENG is a more favorable choice than an EMG.

Here we report a systematic comparative study on low-frequency mechanical energy harvesting by a TENG and an EMG. Both contact-separation (CS) mode and freestanding-sliding (FS) mode of a TENG and an EMG were fabricated for comparison. The open-circuit voltage and short-circuit current of EMG are proportional to the frequency. In contrast, for a TENG, only a short-circuit current is proportional to the frequency, while its open-circuit voltage is high and remains constant. As a result, there always exists a frequency lower than which the output power of a TENG is higher than that of an EMG. The extremely small output voltage of an EMG in the low-frequency range limits its application for driving an electronic unit or charging a battery because each of them has a threshold voltage ( $\sim 0.2$ – $4$  V) for proper operations, while a TENG has an output voltage of usually more than 10–100 V regardless of the frequency. Our study shows that, for frequencies of less than 3 Hz, the efficiency of a TENG is much higher than that of an EMG for harvesting energy in cases such as human motions and possibly ocean waves.

## RESULTS AND DISCUSSION

Currently, four basic modes of TENG operation have been developed, namely, contact-separation (CS) mode,<sup>32</sup> lateral-sliding (LS) mode,<sup>33,34</sup> single-electrode (SE) mode,<sup>35,36</sup> and freestanding-triboelectrification-layer (FT) mode.<sup>21,23</sup> According to the figures-of-merit (FOMs) of a TENG established recently, the structural FOMs of the CS mode and FT mode are dramatically better than that of the other two modes.<sup>37</sup> Hence, these two modes are widely used in varieties of structural designs of TENGs due to the outstanding output performance.<sup>38–40</sup> In the FT mode TENGs, the freestanding-sliding (FS) mode<sup>23</sup> rather than the freestanding-contact (FC) mode<sup>21</sup> is much more widely used practically due to its feasibility to harvest energy available in most external mechanical motions. In analogy, the basic operations of the CS mode<sup>11,14,18</sup> and FS mode<sup>16,41</sup> have also been developed for EMGs for powering small electronics. Therefore, our study was conducted based on the CS mode and FS mode for systematic comparisons between TENGs and EMGs.

As illustrated in [Figure 1a](#), a CS mode EMG was achieved by contact separation between one set of copper (Cu) coils and one piece of square magnet (unless specifically noted). Similarly, a CS mode TENG was fabricated by depositing Cu electrodes on two pieces of fluorinated ethylene propylene (FEP) film, with the Cu side of one film facing the FEP side of the other film for triboelectrification. In [Figure 1b](#), the FS mode EMG was fabricated by placing two sets of copper coils (wound in opposite directions) next to each other, with one piece of square magnet moving horizontally above them. With a similar configuration, in the FS mode TENG, there are two areas of Cu film deposited in parallel next to each other, while one piece of FEP film was used as the triboelectric layer moving horizontally above them. The detailed fabrication process is described in the [Experimental Methods](#) section.

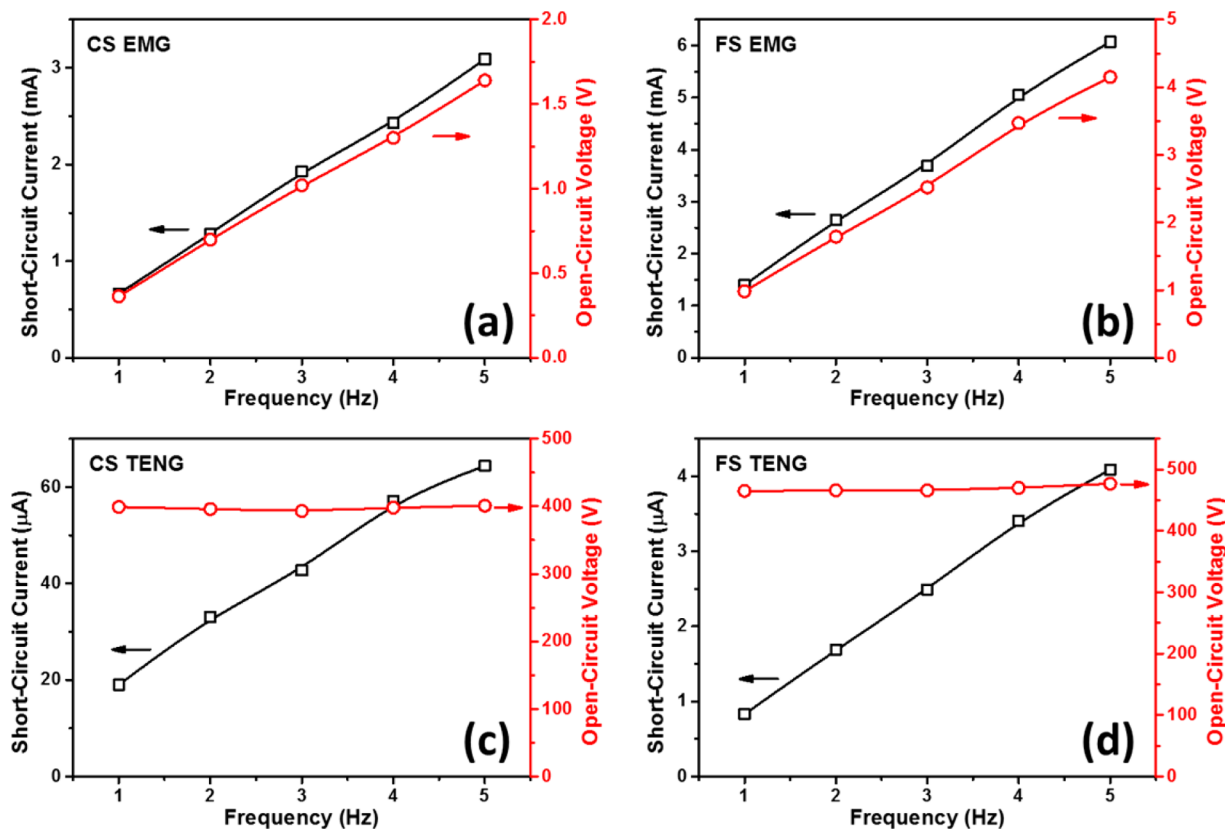


Figure 2. Measured short-circuit currents and open-circuit voltages of the (a) CS mode and (b) FS mode of an EMG and (c) CS mode and (d) FS mode of a TENG.

We first measured both the open-circuit voltages and short-circuit currents for CS and FS modes of the EMG and TENG when they are subjected to various operation frequency, respectively, as shown in Figure 2. The triggered periodical mechanical motion is described in eq 13 in the Experimental Methods section.

According to Faraday's law of electromagnetic induction, the open-circuit voltage of the EMG is proportional to the changing rate of the magnetic flux in each Cu wire loop ( $\Phi$ ) multiplying the number of loops ( $N$ ) in each coil, and the short-circuit current equals the open-circuit voltage over the internal resistance ( $r$ ) of the coils. Their equations (as created by each coil) are expressed as below:<sup>30</sup>

$$V_{OC}^{EMG} = -N \frac{d\Phi}{dt} \quad (1)$$

$$I_{SC}^{EMG} = \frac{V_{OC}^{EMG}}{r} \quad (2)$$

Specifically, for the FS mode EMG, the change of  $\Phi$  is mainly due to the effective area with the parallel magnetic field  $B$  below the magnet. If we assume the majority of the output is determined by the parallel magnetic field  $B$  across the coils, the average absolute open-circuit voltage in this case can be further derived as

$$|V_{OC}^{FS-EMG}| = 4NBSf \quad (3)$$

Here,  $S$  is the average area of each coil, and  $f = 1/T$  ( $T$  as the period) is the frequency of the mechanical motion. The number 4 is added since there are two sets of coils wound in opposite directions and in one period the total magnetic flux changes

twice (from  $BS$  to 0 and from 0 to  $BS$ ). For the CS mode EMG, the change of  $\Phi$  is due to the magnetic field intensity decaying/strengthening with an increase/decrease of the distance from the magnet to the coil, with a period of  $T$ . Similarly, this variation of the magnetic field is also proportional to the frequency of the motions. Therefore, in an EMG, both the open-circuit voltage and the short-circuit current are proportional to the triggering frequency  $f$ , which is consistent with the experimental results shown in Figure 2 a and b.

The operation of a TENG is based on coupling triboelectrification and electrostatic induction.<sup>6–9,37</sup> Initially, a physical contact between at least one pair of triboelectric layers made from different materials creates opposite charges on two surfaces in contact. Then as triggered by mechanical force, relative motion between these layers breaks the existing electrostatic balance, which builds a potential difference between the electrodes and drives free electrons in the electrodes to flow to rebalance the electrostatic field. When the layers move back, the electrons flow back to return to the original equilibrium. Under periodical external mechanical motions, pulsed ac output is delivered. The open-circuit voltage of a TENG for all the modes was derived according to<sup>37</sup>

$$V_{OC}^{TENG} = \frac{Q_{SC}}{C(x)} \quad (4)$$

where  $Q_{SC}$  is the short-circuit charge transfer amount and  $C(x)$  is the capacitance between two electrodes subject to various displacement  $x$ . For any TENG, with the fixed displacement range from 0 to  $x_{max}$ , the maximum charge transfer amount is kept at  $Q_{SC,max} = Q_{SC}(x = x_{max})$ , which is proportional to the triboelectric surface charge density ( $\sigma$ ) and triboelectric surface

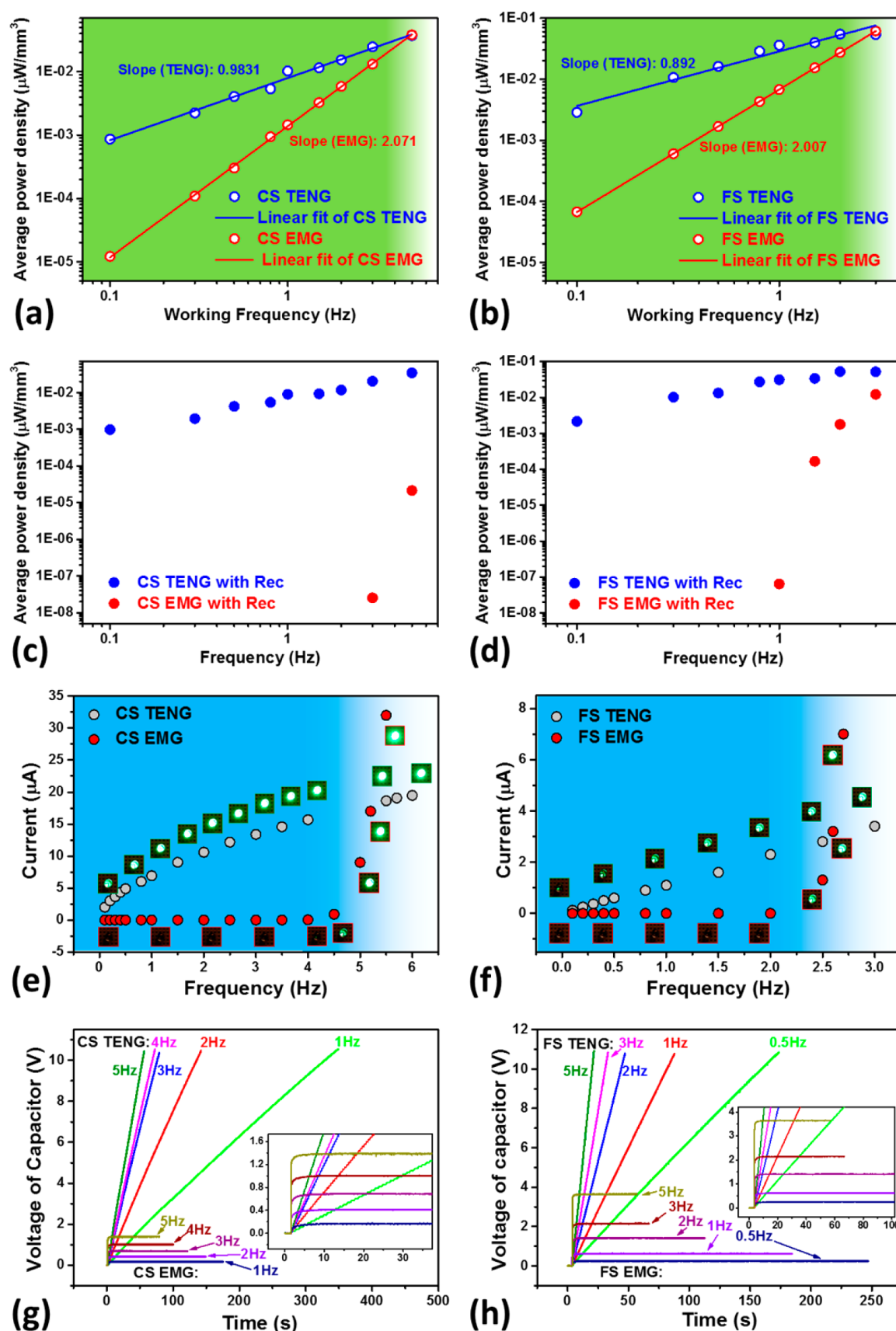


Figure 3. Output performance comparison between an EMG and TENG at low frequency. (a and b) Average power densities  $P$  of (a) CS mode and (b) FS mode devices *versus* frequency  $f$ , with linear fits of  $\log_{10} P$  vs  $\log_{10} f$ . The fitted slopes for the TENG are both about 1, while those for the EMG are both about 2, which means there is always a low-frequency range in which the TENG is able to output a larger power than the EMG, as denoted by the green areas. (c and d) Average rectified power densities of (c) CS mode and (d) FS mode devices. For the



Figure 3. continued

TENG, the power densities with the rectifier are almost the same as that without the rectifier, while for the EMG the rectified power densities decay greatly due to the low output voltages. (e and f) Current through an LED as driven by (e) CS mode and (f) FS mode devices with photos of the lighting LED for a visual indication of the generated power. The blue areas denote the frequency range in which the TENG is more efficient for lighting the LED. The EMG used in (e) has two stacked square magnets. (g and h) Voltage of capacitors as charged by (g) CS mode (a 10  $\mu\text{F}$  capacitor is used) and (h) FS mode (a 3  $\mu\text{F}$  capacitor is used) devices, which shows the saturation voltages as charged by the EMG are limited by the low-voltage output.

area ( $S$ ).<sup>37,42</sup>  $C(x)$  is related only to the structures/dimensions of the TENGs. Therefore, the peak values of the open-circuit voltages should be independent of frequency. As shown in Figure 2c and d, the measured open-circuit voltages of our CS and FS mode TENGs remain at about 400 and 470 V with various frequencies, respectively.

The short-circuit current of a TENG for all the modes is determined by the variation rate of  $Q_{\text{SC}}$ :<sup>37</sup>

$$I_{\text{SC}}^{\text{TENG}} = \frac{dQ_{\text{SC}}}{dt} \quad (5)$$

As stated above,  $Q_{\text{SC,max}}$  is a fixed value.<sup>37</sup> Therefore, the average short-circuit current is derived as  $\overline{I_{\text{SC}}^{\text{TENG}}} = \frac{\int_0^T I_{\text{SC}}^{\text{TENG}} dt}{T} = \frac{2Q_{\text{SC,max}}}{T} = 2Q_{\text{SC,max}}f$ , which is proportional to the triggering frequency  $f$ . (The number 2 is added since the charge transfer changes from 0 to  $Q_{\text{SC,max}}$  and then from  $Q_{\text{SC,max}}$  to 0 in one period  $T$ .) Specifically, for the CS mode, by assuming a uniform motion with average velocity  $v$ , the absolute short-circuit current is given by<sup>43</sup>

$$|I_{\text{SC}}^{\text{CS-TENG}}| = \frac{S\sigma d_0 v}{(d_0 + x)^2} = \frac{2S\sigma d_0 x_{\text{max}}}{(d_0 + x)^2} f \quad (6)$$

where  $d_0$  is the effective thickness of the dielectric layer defined as  $d_0 = \sum d_i/\epsilon_i$ .<sup>43</sup> The peak value of eq 6 is given as about  $[2S\sigma x_{\text{max}}/d_0]f$ , and the average value is calculated as

$$\overline{|I_{\text{SC}}^{\text{CS-TENG}}|} = \frac{\int_0^T \frac{2S\sigma d_0 x_{\text{max}}}{(d_0 + 2x_{\text{max}}ft)^2} f dt}{T} = \frac{2S\sigma x_{\text{max}}}{d_0 + x_{\text{max}}} f \quad (7)$$

For the FS mode, the average absolute short-circuit current is given by (the minimum gap between the electrodes is ignored)<sup>44</sup>

$$\overline{|I_{\text{SC}}^{\text{FS-TENG}}|} = 2\sigma S f \quad (8)$$

From eqs 6–8, we noticed that the short-circuit current of a TENG is proportional to the triggering frequency, which is consistent with the experimental results shown in Figure 2c and d.

To evaluate and compare the overall energy output capability for the EMG and TENG, the optimized average output powers subjected to the matched external load resistance were measured. Theoretically, as a voltage source with a small internal resistance  $r$ ,<sup>31</sup> the output power subjected to external resistance  $R$  can be directly calculated through the following equation:

$$P^{\text{EMG}} = \left( \frac{V_{\text{OC}}^{\text{EMG}}}{R + r} \right)^2 R \quad (9)$$

The optimized average power is given when  $R = r$ , which is

$$P_{\text{opt}}^{\text{EMG}} = \frac{(V_{\text{OC}}^{\text{EMG}})^2}{4r} \quad (10)$$

As we discussed and measured previously, the open-circuit voltage of the EMG is proportional to the triggering frequency  $f$ . Therefore, the optimized average power of the EMG is proportional to the square of the frequency, which is consistent with the previous report<sup>10</sup> ( $C$  is a constant):

$$P_{\text{opt}}^{\text{EMG}} \propto f^2 \text{ or } \log_{10} P_{\text{opt}}^{\text{EMG}} = 2\log_{10} f + C \quad (11)$$

For the TENG, as we stated and demonstrated above, the maximum open-circuit voltage and maximum short-circuit charge transfer both remain constant at various frequencies. Therefore, the largest possible harvested energy per cycle  $E_m$  in the cycle of maximized energy output (CMEO) remains the same for different frequencies, which makes the largest possible average power output proportional to the frequency.<sup>37</sup> The output power directly subjected to the external load resistance, called the cycle of energy output (CEO),<sup>37</sup> is demonstrated to be more complex as related to multiple factors such as the type of mechanical motion, the waiting time at  $x = 0$  or  $x_{\text{max}}$ , etc.<sup>37,43,44</sup> However, as shown in previous simulations for various TENGs,<sup>42–44</sup> the optimized output powers of the CEO at the matched resistance are also approximately proportional to the frequency, which means ( $D$  is a constant different from  $C$ ):

$$\begin{aligned} \overline{P_{\text{opt}}^{\text{TENG}}} &\propto f \text{ or } \log_{10} \overline{P_{\text{opt}}^{\text{TENG}}} \\ &= \log_{10} f + D \text{ (approximately)} \end{aligned} \quad (12)$$

We experimentally demonstrated correlations between the optimized average output power density (of volume) and the frequency for the EMG and TENG fabricated, as shown in Figure 3a (for CS mode) and 3b (FS mode). The methods for measuring and calculating the optimized average powers are described in the Experimental Methods section, and the average power versus external resistance plots are shown in Figure S1, Supporting Information, in which the high output impedance of the TENG can be lowered by a recently reported power-management system.<sup>45</sup> We performed linear fits for logarithms of average power densities versus logarithms of frequencies for both CS and FS modes. As we noted, the fitted slopes for TENGs are both about 1, while those for EMGs are both about 2, which are consistent with the theoretical predictions in eqs 11 and 12. The difference in the fitted slopes indicates there is always a low-frequency range in which the output performance of a TENG is better than that of an EMG, no matter which modes of the TENG and EMG are chosen for comparison. The frequency at which the optimized average power densities for TENG and EMG are equal can be named as the threshold frequency ( $f_{\text{th}}$ ), and the frequency range below  $f_{\text{th}}$  can be called the TENG-dominant frequency range. In our experiments as

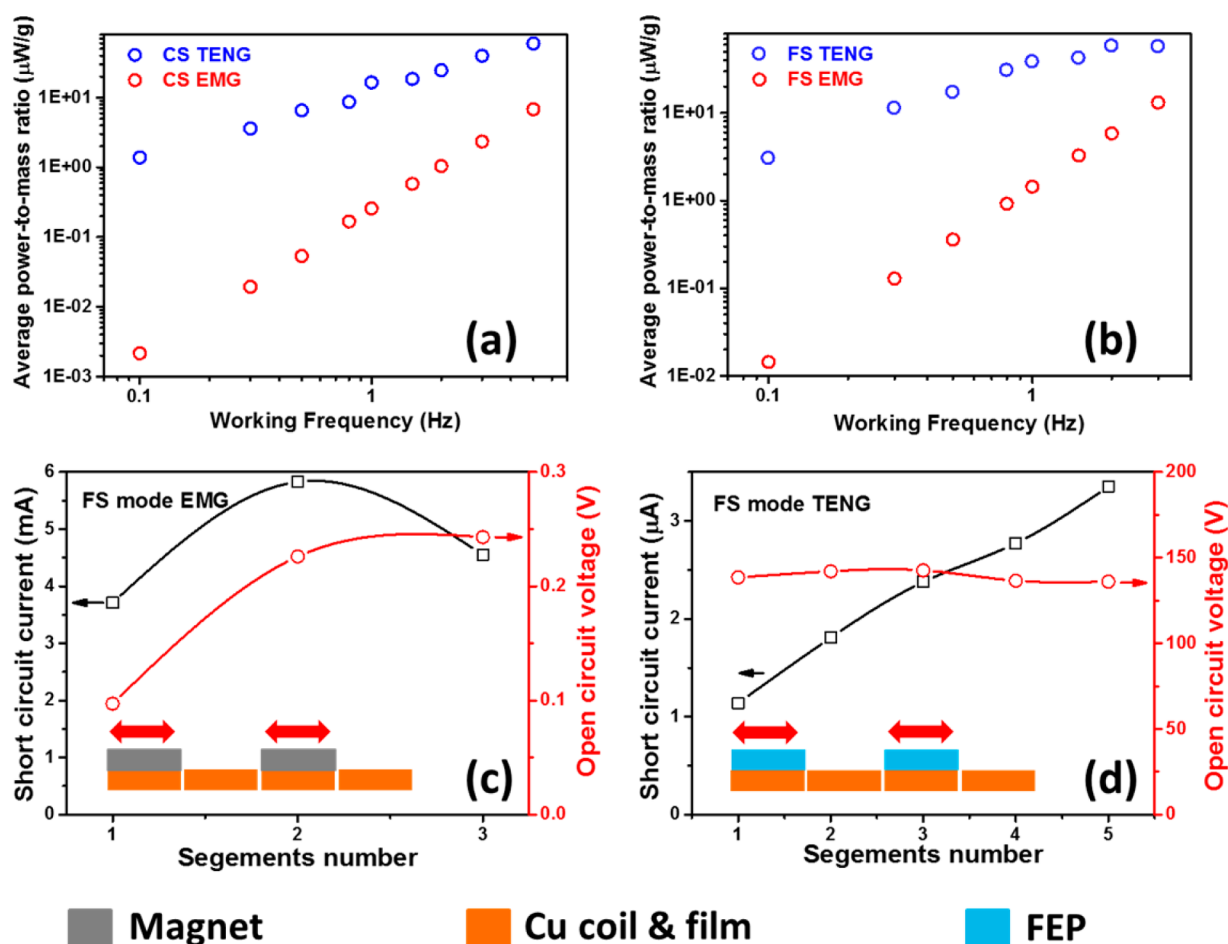


Figure 4. Average power-to-mass ratio of (a) the CS mode and (b) the FS mode of an EMG and TENG, respectively, and the short-circuit currents and open-circuit voltages of the FS mode (c) EMG and (d) TENG with different device structure segmentation number. The insets of (c) and (d) are the schematic diagrams for the EMG and TENG with a segmentation number  $N = 2$ , with the legend shown below the figure.

shown in Figure 3a and b,  $f_{th}$  for fabricated CS and FS mode devices is about 5 and 3 Hz, respectively.

The efficient usage of the energy generated by the EMG and TENG is distinctly different at low frequency. Generally, a series of electronic units are utilized to rectify, regulate, manage, and store the ac power outputs from the EMG and TENG as required for practical applications. Each of these electronic units demands a certain threshold voltage for proper operation. Therefore, the extremely small voltage output of the EMG under low-frequency operation limits its practical applications. Taking the most commonly used full-wave bridge rectifier as an example, each rectifier takes 0.2–0.8 V in the voltage drop, while the diodes inside are working properly. For TENG, due to its high voltage ( $\sim 100$  V level) and low current ( $\sim 10$   $\mu\text{A}$  level) output, this voltage drop is negligible and the power loss is very little. But for the EMG as a low-voltage ( $\sim 1$  V level) and high current ( $\sim 1$  mA level) generator, this voltage drop is relatively large and the power loss is huge, especially for the low-frequency range. We experimentally measured the optimized output power densities of the EMG and TENG using the rectifier, as shown in Figure 3c and d. As we noted, the optimized output power densities for both CS and FS mode TENGs using the rectifier are almost the same as those without using the rectifier (as in Figure 3a and b), indicating little power loss due to rectification. But for the EMG, the power densities after using the rectifier are rather small. With an even lower

frequency range ( $<3$  Hz for the CS mode and  $<1$  Hz for the FS mode), the output power densities become too small to be measured, which shows the ineffectiveness of EMG for harvesting low-frequency energy.

The low output voltage of the EMG at low frequency largely reduces the effective usage of its generated power. To further demonstrate the disadvantage of the low voltage from EMG in low-frequency energy harvesting for powering small electronics, we utilized an EMG and TENG to power an LED (with an  $I$ – $V$  curve as shown in Figure S2, Supporting Information) and charge capacitors (10  $\mu\text{F}$  for the CS mode and 3  $\mu\text{F}$  for the FS mode) under low-frequency motions. As measured, the minimum voltage required for lighting the LED is about 2.3 V, while the current required is less than 1  $\mu\text{A}$ , which can be very easily satisfied by the TENG, even at a quite low frequency of  $\sim 0.1$  Hz. However, for the EMG under low-frequency motions, a certain frequency is required to achieve the required minimum voltage ( $\sim 4.5$  Hz for the CS mode EMG with two stacked square magnets and  $\sim 2.5$  Hz for the FS mode EMG as measured). The difference in the required minimum frequencies for the EMG and TENG is shown in Figure 3e and f. The voltages of the capacitors as charged by the EMG and TENG are shown in Figure 3g and h. During charging the capacitors by EMGs through the rectifier, the saturation voltage, which is defined as the highest possible voltage achieved,<sup>46</sup> is limited by the low open-circuit voltages (usually

less than 2 V for  $f < 3$  Hz). Because of the low saturation voltage, most of the energy from the EMG cannot be stored and is largely lost! Besides, this limitation makes the EMG unable to charge an energy storage unit that operates at a higher voltage. For example, to charge a common lithium-ion coin cell battery, usually at least 3–4 V in voltage is required. For a TENG, it has been demonstrated that the voltage of the capacitors can be charged up to the maximum open-circuit voltage (for the designed charging cycle),<sup>47</sup> which is usually more than 10–100 V. Besides, the rate of using a TENG to charge a battery/capacitor can be greatly enhanced through the designed charging cycle<sup>47</sup> and the power-management system<sup>45</sup> as reported.

In practical applications for ambient mechanical energy harvesting, the TENG also benefits from several other advantages. One of them is the light weight of the fabricated device since it requires only a few layers of polymer films with electrodes. As a comparison, the EMG as composed by magnets and metal coils is dramatically heavy. Figure 4a and b give the optimized average power-to-mass ratio for both the EMG and TENG. Due to the great difference in the weight under an equivalent volume, the average power-to-mass ratio of the TENG is much better than that of the EMG in an even larger frequency range. The light weight but great power output of the TENG makes it a perfect candidate for wearable and implantable applications, which however cannot be achieved by the EMG.

The output performance of the TENG can be easily scaled up through advanced structure designs such as grating structures<sup>27,34</sup> and multilayer structures.<sup>48,49</sup> For example, by dividing the FS mode TENG into the linear grating structure, the output performance can be further enhanced, and it can be used to harvest mechanical energy with minimum displacement.<sup>27</sup> Here we fabricated the FS mode TENGs with the number of subdivisions  $N$  from 1 to 5. Similar structures with subdivisions of the FS mode EMG were also fabricated for comparison. The schematic diagrams of a subdivided EMG and TENG (both with  $N = 2$ ) are shown in the insets of Figure 4c and d. For the TENG, with different numbers of subdivisions, the open-circuit voltage was measured to be approximately the same. With the increase of  $N$ , the time slot to transfer  $Q_{SC,max}$  is decreased as  $\frac{T}{2N}$ , and hence the short-circuit current as well as the output power increases,<sup>27</sup> as consistent with the experimental results in Figure 4d. This strategy can also be altered to be a rotational grating structure with outstanding output performance brought by subdivisions with submillimeter width,<sup>39,50</sup> demonstrating the grating structure as an effective strategy for greatly enhancing the output performance of the TENG. For the EMG with an increased number of subdivisions, as the total number of Cu wire loops increases, the open-circuit voltage increases. However, since the magnetic fields from different magnets influence each other, once the magnets become more numerous, the increase of the open-circuit voltage will saturate eventually. In our experiments as shown in Figure 4c, after  $N = 2$ , the increase of the open-circuit voltage begins to saturate. Moreover, due to the dramatic increase of the internal resistance  $r$ , the short-circuit current starts to decrease at  $N = 3$ , which is not favorable. Such influences from magnetic fields and internal resistance on the performance cannot happen in TENGs with advanced designs. Therefore, as compared with an EMG, the TENG is a much better choice to harvest mechanical energy with the possibility

to achieve enhanced output performance through advanced structure designs.

## CONCLUSION

In summary, low-frequency mechanical energy harvesting by an EMG and TENG is studied systematically. The output characteristics of an EMG are low voltage and high current, and both the open-circuit voltage and the short-circuit current are proportional to the mechanical triggering frequency. For the TENG, with high voltage and low current, the open-circuit voltage remains constant and the short-circuit current is proportional to the frequency. These characteristics make the output power of the TENG high and even much higher than that of an EMG below a certain threshold frequency, called the TENG-dominant frequency range ( $<5$  Hz for the CS mode and  $<3$  Hz for the FS mode as measured). This threshold frequency always exists while comparing any TENGs and any EMGs. Besides, as operated in the low-frequency range, the extremely small output voltage of the EMG limits its applications for driving electronics units such as a rectifier and an LED or charging a battery, since each of them requires a threshold voltage of  $\sim 0.2$ –4 V for proper operation. Furthermore, the TENG also shows advantages of light weight and the possibility to enhance the performance through advanced structure designs. All these characteristics make the TENG a possible killer application to harvest sub-3 Hz frequency mechanical energy such as human motions for powering small electronics or possibly ocean waves for large-scale power generation (blue energy).

## EXPERIMENTAL METHODS

**Preparation of the CS Mode TENG and EMG.** For TENG fabrication, typically, a 1.5 mm acrylic sheet was cut into two square pieces ( $30 \times 30$  mm) by a laser cutter (PLS 6.75, Universal Laser Systems) as the substrate. Both of the square sheets were abraded by fine grit sandpaper (#5000) to ensure a flat working surface. Two FEP films ( $25 \times 25$  mm, thickness of 100  $\mu\text{m}$ ) were prepared by depositing Cu electrode (200 nm by PVD 500) on one side of each film. Then, the two as-prepared FEP films were pasted onto the square substrates to make the FEP surface of one deposited film face the Cu surface of the other film. The total TENG is about 1450  $\text{mm}^3$  in volume and 0.9 g in weight.

For EMG fabrication, a 3.0 mm acrylic sheet ( $10 \times 10$  mm) was sandwiched by two 1.5 mm acrylic sheets ( $30 \times 30$  mm) as a frame. Then, Cu wire with a diameter of 0.08 mm was wound in the frame as the coil. Each coil has 1200 loops. Finally, in this experiment, one (two for lighting the LED) square neodymium–iron–boron magnet(s) (1 in. long, 1 in. wide, 0.1 in. thick, 8 lbs maximum pull) was used to contact and separate the coil to generate output. This TENG is about 3750  $\text{mm}^3$  in volume and 21.04 g in weight.

**Preparation of the FS Mode TENG and EMG.** For TENG fabrication, a 1.5 mm acrylic sheet was cut into two pieces; one is  $30 \times 30$  mm in size, and the other is  $55 \times 30$  mm in size. Both of them were abraded by fine grit sandpaper (#5000) to ensure a flat working surface. Then the acrylic sheet with a size of  $55 \times 30$  mm was deposited with two 500 nm Cu electrodes ( $25 \times 25$  mm) with an interval of 1 mm after predepositing 50 nm of titanium (Ti) as a buffer layer using a PVD 500. Then a piece of FEP film ( $25 \times 25$  mm, thickness of 100  $\mu\text{m}$ ) was pasted to the other acrylic sheet as the triboelectric layer. This TENG is 2062  $\text{mm}^3$  in volume and 1.95 g in weight.

For EMG fabrication, two 3.0 mm acrylic sheets ( $10 \times 10$  mm) were sandwiched by four 1.5 mm acrylic sheets ( $28 \times 30$  mm) to form two frames. Then, Cu wire with a 0.08 mm diameter was wound in the two frames, and the winding directions of the coils in the two frames were opposite. Each coil in the EMG has 1200 loops except the one



with subdivisions. Finally, a square neodymium–iron–boron magnet (1 in. long, 1 in. wide, 0.1 in. thick, 8 lbs maximum pull) moves horizontally above the Cu coils to generate output. This EMG is about 6250 mm<sup>3</sup> in volume and 29.35 g in weight.

For the FS mode EMG and TENG with subdivisions, the total size of the devices is 60 × 30 mm, and they are divided equally for different numbers of subdivisions. The magnets used here are ultra-high-pull stretchable magnets made by neodymium–iron–boron bonded with synthetic rubber, which can be easily cut into pieces. The size of the magnets/FEP films were cut properly to fit the size of each Cu coil/electrode. Each coil in the EMG used here has 100 loops.

**Electrical Measurement.** The output voltage and current of the devices were measured via a voltage preamplifier (Keithley 6514 system electrometer). The software platform was constructed based on LabVIEW, which is capable of realizing real-time data acquisition control and analysis.

**Applied Mechanical Motion.** A linear motor was used in this experiment to produce the motion with various frequencies. The set motion in each period (as started from  $t = 0$ ) is described by the following equation:

$$x = \begin{cases} 8x_{\max}f^2t^2, & 0 \leq t \leq \frac{1}{4f} \\ 8x_{\max}ft - 8x_{\max}f^2t^2 - x_{\max}, & \frac{1}{4f} \leq t \leq \frac{3}{4f} \\ 8x_{\max}f^2\left(\frac{1}{f} - t\right)^2, & \frac{3}{4f} \leq t \leq \frac{1}{f} \end{cases} \quad (13)$$

**Measurement and Calculations to Determine the Optimized Average Power Output.** For both the TENG and EMG connected with various external load resistances, the voltage across the resistance and the current flowing through the resistance were measured simultaneously. The schematic diagrams for measurement circuits without and with the rectifier are shown in Figure S3, [Supporting Information](#). Then the average output powers were calculated as ( $t_0$  is a randomly picked time during operations)

$$\overline{P^{\text{TENG}}} = \frac{\int_{t_0}^{t_0+T} VI \, dt}{T} \quad (14)$$

The average power outputs *versus* resistances were plotted in Figure S1, [Supporting Information](#). Finally the highest power for each frequency was used to calculate the optimized average power density and power-to-mass ratio, and the resistance with respect to the highest power is the matched load resistance. The optimized average powers with the rectifier were measured directly at the matched load resistance.

## ASSOCIATED CONTENT

### Supporting Information

The Supporting Information is available free of charge on the ACS Publications website at DOI: 10.1021/acsnano.6b01569.

Figures S1–S3 ([PDF](#))

## AUTHOR INFORMATION

### Corresponding Author

\*E-mail: [zhong.wang@mse.gatech.edu](mailto:zhong.wang@mse.gatech.edu).

### Author Contributions

<sup>‡</sup>Y. Zi, H. Guo, and Z. Wen contributed equally to this work.

### Notes

The authors declare no competing financial interest.

## ACKNOWLEDGMENTS

The research was supported by the Hightower Chair Foundation and the “Thousands Talents” Program for Pioneer Researcher and His Innovation Team, China.

## REFERENCES

- (1) Wang, Z. L. Self-Powered Nanotech. *Sci. Am.* **2008**, 298, 82–87.
- (2) El-hami, M.; Glynne-Jones, P.; White, N. M.; Hill, M.; Beeby, S.; James, E.; Brown, A. D.; Ross, J. N. Design and Fabrication of a New Vibration-Based Electromechanical Power Generator. *Sens. Actuators, A* **2001**, 92, 335–342.
- (3) Jefimenko, O. D.; Walker, D. K. Electrostatic Current Generator Having a Disk Electret as an Active Element. *IEEE Trans. Ind. Appl.* **1978**, IA-14, 537–540.
- (4) Fan, F.-R.; Tian, Z.-Q.; Wang, Z. L. Flexible Triboelectric Generator. *Nano Energy* **2012**, 1, 328–334.
- (5) Wang, Z. L.; Song, J. Piezoelectric Nanogenerators Based on Zinc Oxide Nanowire Arrays. *Science* **2006**, 312, 242–246.
- (6) Wang, Z. L. Triboelectric Nanogenerators as New Energy Technology for Self-Powered Systems and as Active Mechanical and Chemical Sensors. *ACS Nano* **2013**, 7, 9533–9557.
- (7) Wang, Z. L. Triboelectric Nanogenerators as New Energy Technology and Self-Powered Sensors - Principles, Problems and Perspectives. *Faraday Discuss.* **2014**, 176, 447.
- (8) Wang, Z. L.; Chen, J.; Lin, L. Progress in Triboelectric Nanogenerators as a New Energy Technology and Self-Powered Sensors. *Energy Environ. Sci.* **2015**, 8, 2250–2282.
- (9) Zhu, G.; Bai, P.; Chen, J.; Jing, Q.; Wang, Z. L. Triboelectric Nanogenerators as a New Energy Technology: From Fundamentals, Devices, to Applications. *Nano Energy* **2015**, 14, 126–138.
- (10) Kulah, H.; Najafi, K. In *An Electromagnetic Micro Power Generator for Low-Frequency Environmental Vibrations*, 17th IEEE International Conference on Micro Electro Mechanical Systems (MEMS), 2004, 2004; pp 237–240.
- (11) Abu Riduan, M. F.; Gwi-Sang, C. Fabrication and Characterization of a Low Frequency Electromagnetic Energy Harvester. *J. Semicond.* **2012**, 33, 074001.
- (12) Zorlu, O.; Topal, E. T.; Kulah, H. A Vibration-Based Electromagnetic Energy Harvester Using Mechanical Frequency Up-Conversion Method. *IEEE Sens. J.* **2011**, 11, 481–488.
- (13) Rahimi, A.; Zorlu, Ö.; Muhtaroglu, A.; Kulah, H. An Electromagnetic Energy Harvesting System for Low Frequency Applications with a Passive Interface ASIC in Standard CMOS. *Sens. Actuators, A* **2012**, 188, 158–166.
- (14) Aw, K. C.; Praneeth, S. V. In *Low Frequency Vibration Energy Harvesting from Human Motion Using IPMC Cantilever with Electromagnetic Transduction*; 8th IEEE International Conference on Nano/Micro Engineered and Molecular Systems (NEMS), April 7–10, 2013; 2013; pp 645–648.
- (15) Choi, Y.; Ju, S.; Chae, S. H.; Jun, S.; Park, S. M.; Lee, S.; Lee, H. W.; Ji, C. H. Low Frequency Vibration Energy Harvester Using Spherical Permanent Magnet with Non-uniform Mass Distribution. *J. Phys.: Conf. Ser.* **2013**, 476, 012123.
- (16) Chae, S. H.; Ju, S.; Choi, Y.; Jun, S.; Park, S. M.; Lee, S.; Lee, H. W.; Ji, C. H. Electromagnetic Vibration Energy Harvester Using Springless Proof Mass and Ferrofluid as a Lubricant. *J. Phys.: Conf. Ser.* **2013**, 476, 012013.
- (17) Soon-Duck, K.; Jinkyoo, P.; Kincho, L. Electromagnetic Energy Harvester with Repulsively Stacked Multilayer Magnets for Low Frequency Vibrations. *Smart Mater. Struct.* **2013**, 22, 05S007.
- (18) Sun, W.; Jung, J.; Seok, J. Frequency-Tunable Electromagnetic Energy Harvester using Magneto-Rheological Elastomer. *J. Intell. Mater. Syst. Struct.* **2016**, 27, 959.
- (19) Chen, J.; Zhu, G.; Yang, W.; Jing, Q.; Bai, P.; Yang, Y.; Hou, T.-C.; Wang, Z. L. Harmonic-Resonator-Based Triboelectric Nanogenerator as a Sustainable Power Source and a Self-Powered Active Vibration Sensor. *Adv. Mater.* **2013**, 25, 6094–6099.



- (20) Yang, J.; Chen, J.; Yang, Y.; Zhang, H.; Yang, W.; Bai, P.; Su, Y.; Wang, Z. L. Broadband Vibrational Energy Harvesting Based on a Triboelectric Nanogenerator. *Adv. Energy Mater.* **2014**, 410.1002/aenm.201301322.
- (21) Wang, S.; Niu, S.; Yang, J.; Lin, L.; Wang, Z. L. Quantitative Measurements of Vibration Amplitude Using a Contact-Mode Freestanding Triboelectric Nanogenerator. *ACS Nano* **2014**, 8, 12004–12013.
- (22) Yang, W.; Chen, J.; Zhu, G.; Yang, J.; Bai, P.; Su, Y.; Jing, Q.; Cao, X.; Wang, Z. L. Harvesting Energy from the Natural Vibration of Human Walking. *ACS Nano* **2013**, 7, 11317–11324.
- (23) Wang, S.; Xie, Y.; Niu, S.; Lin, L.; Wang, Z. L. Freestanding Triboelectric-Layer-Based Nanogenerators for Harvesting Energy from a Moving Object or Human Motion in Contact and Non-contact Modes. *Adv. Mater.* **2014**, 26, 2818–2824.
- (24) Zhong, J.; Zhang, Y.; Zhong, Q.; Hu, Q.; Hu, B.; Wang, Z. L.; Zhou, J. Fiber-Based Generator for Wearable Electronics and Mobile Medication. *ACS Nano* **2014**, 8, 6273–6280.
- (25) Seung, W.; Gupta, M. K.; Lee, K. Y.; Shin, K.-S.; Lee, J.-H.; Kim, T. Y.; Kim, S.; Lin, J.; Kim, J. H.; Kim, S.-W. Nanopatterned Textile-Based Wearable Triboelectric Nanogenerator. *ACS Nano* **2015**, 9, 3501–3509.
- (26) Kim, K. N.; Chun, J.; Kim, J. W.; Lee, K. Y.; Park, J.-U.; Kim, S.-W.; Wang, Z. L.; Baik, J. M. Highly Stretchable 2D Fabrics for Wearable Triboelectric Nanogenerator under Harsh Environments. *ACS Nano* **2015**, 9, 6394–6400.
- (27) Xie, Y.; Wang, S.; Niu, S.; Lin, L.; Jing, Q.; Yang, J.; Wu, Z.; Wang, Z. L. Grating-Structured Freestanding Triboelectric-Layer Nanogenerator for Harvesting Mechanical Energy at 85% Total Conversion Efficiency. *Adv. Mater.* **2014**, 26, 6599–6607.
- (28) Chen, J.; Yang, J.; Li, Z.; Fan, X.; Zi, Y.; Jing, Q.; Guo, H.; Wen, Z.; Pradel, K. C.; Niu, S.; Wang, Z. L. Networks of Triboelectric Nanogenerators for Harvesting Water Wave Energy: A Potential Approach toward Blue Energy. *ACS Nano* **2015**, 9, 3324–3331.
- (29) Wang, X.; Niu, S.; Yin, Y.; Yi, F.; You, Z.; Wang, Z. L. Triboelectric Nanogenerator Based on Fully Enclosed Rolling Spherical Structure for Harvesting Low-Frequency Water Wave Energy. *Adv. Energy Mater.* **2015**, 510.1002/aenm.201501467.
- (30) Guo, H.; Wen, Z.; Zi, Y.; Yeh, M.-H.; Wang, J.; Zhu, L.; Hu, C.; Wang, Z. L. A Water-Proof Triboelectric–Electromagnetic Hybrid Generator for Energy Harvesting in Harsh Environments. *Adv. Energy Mater.* **2016**, 610.1002/aenm.201501593.
- (31) Zhang, C.; Tang, W.; Han, C.; Fan, F.; Wang, Z. L. Theoretical Comparison, Equivalent Transformation, and Conjunction Operations of Electromagnetic Induction Generator and Triboelectric Nanogenerator for Harvesting Mechanical Energy. *Adv. Mater.* **2014**, 26, 3580–3591.
- (32) Zhu, G.; Pan, C.; Guo, W.; Chen, C.-Y.; Zhou, Y.; Yu, R.; Wang, Z. L. Triboelectric-Generator-Driven Pulse Electrodeposition for Micropatterning. *Nano Lett.* **2012**, 12, 4960–4965.
- (33) Wang, S.; Lin, L.; Xie, Y.; Jing, Q.; Niu, S.; Wang, Z. L. Sliding-Triboelectric Nanogenerators Based on In-Plane Charge-Separation Mechanism. *Nano Lett.* **2013**, 13, 2226–2233.
- (34) Zhu, G.; Chen, J.; Liu, Y.; Bai, P.; Zhou, Y. S.; Jing, Q.; Pan, C.; Wang, Z. L. Linear-Grating Triboelectric Generator Based on Sliding Electrification. *Nano Lett.* **2013**, 13, 2282–2289.
- (35) Yang, Y.; Zhang, H.; Chen, J.; Jing, Q.; Zhou, Y. S.; Wen, X.; Wang, Z. L. Single-Electrode-Based Sliding Triboelectric Nanogenerator for Self-Powered Displacement Vector Sensor System. *ACS Nano* **2013**, 7, 7342–7351.
- (36) Yang, Y.; Zhou, Y. S.; Zhang, H.; Liu, Y.; Lee, S.; Wang, Z. L. A Single-Electrode Based Triboelectric Nanogenerator as Self-Powered Tracking System. *Adv. Mater.* **2013**, 25, 6594–6601.
- (37) Zi, Y.; Niu, S.; Wang, J.; Wen, Z.; Tang, W.; Wang, Z. L. Standards and Figure-of-Merits for Quantifying the Performance of Triboelectric Nanogenerators. *Nat. Commun.* **2015**, 6, 8376.
- (38) Zhu, G.; Zhou, Y. S.; Bai, P.; Meng, X. S.; Jing, Q.; Chen, J.; Wang, Z. L. A Shape-Adaptive Thin-Film-Based Approach for 50% High-Efficiency Energy Generation Through Micro-Grating Sliding Electrification. *Adv. Mater.* **2014**, 26, 3788–3796.
- (39) Zhu, G.; Chen, J.; Zhang, T.; Jing, Q.; Wang, Z. L. Radial-Arrayed Rotary Electrification for High Performance Triboelectric Generator. *Nat. Commun.* **2014**, 5, 3426.
- (40) Kim, S.; Gupta, M. K.; Lee, K. Y.; Sohn, A.; Kim, T. Y.; Shin, K.-S.; Kim, D.; Kim, S. K.; Lee, K. H.; Shin, H.-J.; Kim, D.-W.; Kim, S.-W. Transparent Flexible Graphene Triboelectric Nanogenerators. *Adv. Mater.* **2014**, 26, 3918–3925.
- (41) Herrault, F.; Chang-Hyeon, J.; Allen, M. G. Ultraminiaturized High-Speed Permanent-Magnet Generators for Milliwatt-Level Power Generation. *J. Microelectromech. Syst.* **2008**, 17, 1376–1387.
- (42) Niu, S.; Wang, Z. L. Theoretical Systems of Triboelectric Nanogenerators. *Nano Energy* **2015**, 14, 161–192.
- (43) Niu, S.; Wang, S.; Lin, L.; Liu, Y.; Zhou, Y. S.; Hu, Y.; Wang, Z. L. Theoretical Study of Contact-Mode Triboelectric Nanogenerators as an Effective Power Source. *Energy Environ. Sci.* **2013**, 6, 3576–3583.
- (44) Niu, S.; Liu, Y.; Chen, X.; Wang, S.; Zhou, Y. S.; Lin, L.; Xie, Y.; Wang, Z. L. Theory of Freestanding Triboelectric-Layer-based Nanogenerators. *Nano Energy* **2015**, 12, 760–774.
- (45) Niu, S.; Wang, X.; Yi, F.; Zhou, Y. S.; Wang, Z. L. A Universal Self-Charging System Driven by Random Biomechanical Energy for Sustainable Operation of Mobile Electronics. *Nat. Commun.* **2015**, 6, 8975.
- (46) Niu, S.; Liu, Y.; Zhou, Y. S.; Wang, S.; Lin, L.; Wang, Z. L. Optimization of Triboelectric Nanogenerator Charging Systems for Efficient Energy Harvesting and Storage. *IEEE Trans. Electron Devices* **2015**, 62, 641–647.
- (47) Zi, Y.; Wang, J.; Wang, S.; Li, S.; Wen, Z.; Guo, H.; Wang, Z. L. Effective Energy Storage from a Triboelectric Nanogenerator. *Nat. Commun.* **2016**, 7, 10987.
- (48) Cheng, G.; Zheng, L.; Lin, Z.-H.; Yang, J.; Du, Z.; Wang, Z. L. Multilayered-Electrode-Based Triboelectric Nanogenerators with Managed Output Voltage and Multifold Enhanced Charge Transport. *Adv. Energy Mater.* **2015**, 510.1002/aenm.201401452.
- (49) Xie, Y.; Wang, S.; Niu, S.; Lin, L.; Jing, Q.; Su, Y.; Wu, Z.; Wang, Z. L. Multi-Layered Disk Triboelectric Nanogenerator for Harvesting Hydropower. *Nano Energy* **2014**, 6, 129–136.
- (50) Han, C.; Zhang, C.; Tang, W.; Li, X.; Wang, Z. High Power Triboelectric Nanogenerator Based on Printed Circuit Board (PCB) Technology. *Nano Res.* **2015**, 8, 722–730.